# The role of high cholesterol in age-related COVID19 lethality.

Hao Wang[1,2,3], Zixuan Yuan[1,2,3], Mahmud Arif Pavel[1,2], Scott B. Hansen[1,2,*]

[1]Department of Molecular Medicine, [2]Department of Neuroscience, [3]Skaggs Graduate School of Chemical and Biological Sciences, The Scripps Research Institute, Jupiter, Florida 33458, USA

*Correspondence: shansen@scripps.edu

## ABSTRACT

Coronavirus disease 2019 (COVID19) is a respiratory infection caused by severe acute respiratory syndrome coronavirus 2 (SARS-CoV-2) originating in Wuhan China in 2019. The disease is notably severe in elderly and those with underlying chronic conditions. A molecular mechanism that explains why the elderly are vulnerable and why children are resistant is largely unknown. Understanding these differences is critical for safeguarding the vulnerable and guiding effective policy and treatments. Here we show loading cells with cholesterol from blood serum using the cholesterol transport protein apolipoprotein E (apoE) enhances the endocytic entry of pseudotyped SARS-CoV-2. Super resolution imaging of the SARS-CoV-2 entry point with high cholesterol showed almost twice the total number of viral entry points. The cholesterol concomitantly traffics angiotensinogen converting enzyme (ACE2) to the viral entry site where SARS-CoV-2 docks to properly exploit entry into the cell. Cholesterol also increased binding of SARS-CoV-2 receptor binding domains. In mouse lung we found age and high fat diet induced cholesterol loading into lung tissue by up to 40%. Based on these findings, we propose a cholesterol dependent model for COVID19 lethality in elderly and the chronically ill. As cholesterol increases with age and inflammation (e.g. obesity, smoking, and diabetes), the cell surface is coated with viral entry points, optimally assembled viral entry proteins, and optimal furin priming. Importantly our model suggests problems arise when cholesterol levels are high in the tissue, not the blood. In fact, rapidly dropping cholesterol in the blood may indicate severe loading of cholesterol in peripheral tissue and a dangerous situation for escalated SARS-CoV-2 infectivity. Molecules that remove cholesterol from tissue or disrupt ACE2 localization with viral entry points or furin localization for priming in the producer cells, likely reduce the severity of COVID19 in critically ill patients.

## INTRODUCTION

In early 2020, COVID19 spread rapidly throughout the developed world leading to extensive death and an ongoing pandemic. The lethality of the virus is notably selective for elderly[1,2] and those with chronic disease such as hypertension, diabetes, cardiovascular disease, and smoking[3–5]. Interestingly, almost all children are either asymptomatic or present with very minor symptoms, while elderly and those with underlying conditions experience very severe life-threatening symptoms. This disparity was also observed with SARS-CoV-1, a closely related virus which failed to kill any children under the age of 12, despite being much more lethal than SARS-CoV-2 in adults[6]. Understanding why young people are resistant in this class of viruses could help both healthy and chronically ill adults avoid severe symptoms of COVID19.

The ability of a virus to enter a cell is critical to its lethality. SARS-CoV-2 enters the cell by binding a receptor angiotensinogen converting enzyme 2 (ACE2)[7,8]. Initial theories suggested that the expression level of the ACE2 receptor determined the level of disease severity in children[9]. However, more recent studies in COVID-19 patients show conflicting results and even a paradoxical increase of ACE2 in young children[4,10]. This result raises the question, What controls SARS-CoV-2 entry?

Cholesterol is an insoluble eukaryotic lipid found in membranes throughout the human body, most notably in the plasma membrane. It appears to accumulate in tissue with age[11–13]. Furthermore, chronic inflammation causes cholesterol loading into macrophage rich tissue[14]. Pneumocytes in the lung load and unload cholesterol along with macrophages and this process is associated with lung diease[15] and lung function[16,17]. For further discussion on cholesterol in peripheral tissue see Figure S1B.

Aspects of SARS-CoV-1 entry, a closely related virus, suggests a potential mechanism for

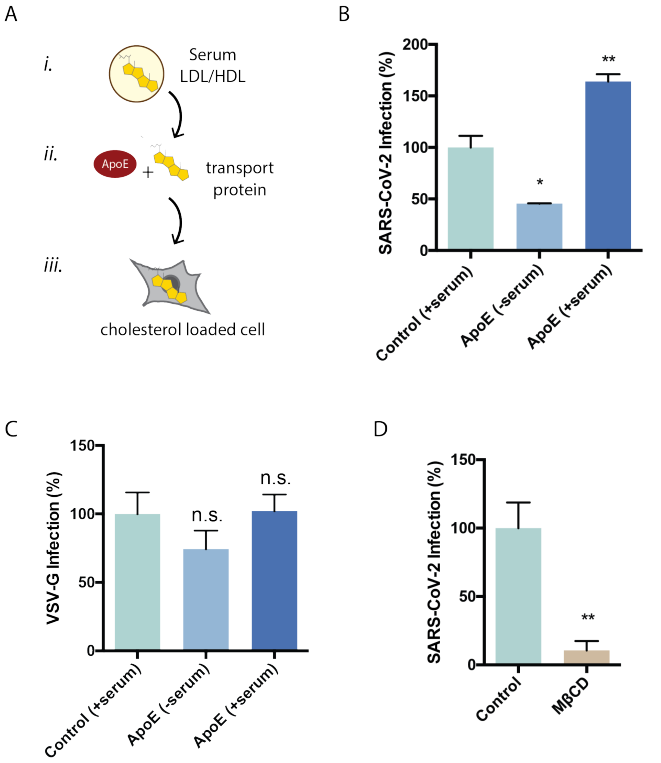


**Figure 1. Cholesterol dependent inhibition of SARS-CoV-2 viral infection** (**A**) Cartoon diagram showing the experimental setup for loading cultured cells with cholesterol. ***i.***, Cholesterol (yellow shading) is shown loaded into lipoprotein (e.g., low- and high-density lipoprotein (LDL and HDL respectively)) from blood serum. ***ii.***, Cholesterol free human apolipoprotein E (apoE, brown shading) a cholesterol transport protein is exposed to mixed with blood serum and ***iii,*** ApoE transports cholesterol in and out of cells (grey shading) (see also Supplemental Figure S1B). (**B**) SARS-CoV-2 pseudovirus (CoV-2-PV) entry assay. Cells were treated with a luciferase expressing retrovirus pseudotyped with the SARS-CoV-2 spike protein that recapitulates viral entry. Infectivity was monitored by a luciferase activity in cells treated with or without apoE. High cholesterol (apoE + serum) was more than 3-fold higher compared to low cholesterol. Data are expressed as mean ± s.e.m., *P<0.05, **P<0.01, one-way ANOVA. (**C**) Pseudotyped control virus, vesicular stomatitis G virus (VSV-G), is not cholesterol dependent, n.s.≥0.05 one-way ANOVA, n=6. (**D**) Depletion of cellular cholesterol with methyl-beta-cyclodextrin (MβCD) blocked almost all viral entry measured by pseudotyped luciferase assay. Data are expressed as mean ± s.e.m., **P<0.01, two-sided Student's t-test.

cholesterols effects. In cultured cells, SARS-CoV-1 is thought to utilize both a cholesterol dependent endocytic pathways through monosialotetrahexosylganglioside1 (GM1) lipid domains and a cell-surface mechanism[18]. Cholesterol is needed to form GM1 lipid rafts (also called GM1 lipid rafts, see Supplemental Figure S1A[19]) used in the endocytic process. Furthermore the cholesterol localizes ACE2 to detergent resistant membranes (DRMs)[20,21] which are similar in composition to GM1 lipid domains but not the same..

We hypothesized that age-dependent SARS-CoV-2 entry depends on cholesterol loading into lung tissue. Here we show that lung cholesterol increases in aged diabetic mice and similar increases of cholesterol traffic ACE2 to a more infectious endocytic pathway.

## RESULTS

### Cholesterol dependent SARS-CoV-2 pseudovirus entry.

To test the cholesterol dependence of SARS-COV-2 on viral entry we loaded cholesterol into HEK293T cells with apolipoprotein E (apoE) and blood serum and treated the cells with retroviruse pseudotyped with the SARS-CoV-2 S protein (CoV-2-PV)[22,23]. A segment of the S protein binds to the ACE2 and recapitulates viral entry[24]. ApoE is a cholesterol carrier protein linked to Alzheimer's and the severity of COVID19[26]. In tissue, ApoE binds to low-density lipoprotein receptor and facilitates loading of cholesterol into cells when bound to lipids (Figure 1A). When lipids are not present, apoE has the opposite effect; it facilitates efflux of cholesterol from the cell[25] (Supplemental Figure S1B). is linked to increased severity of.

We found cholesterol loading (apoE + serum) significantly increased CoV-2-PV entry and cholesterol unloading had the opposite effect. Figure 1B shows CoV-2-PV entry increased 50% compared to control (serum only). Cholesterol was loaded into cells by applying 4 µg/mL apoE and 10% serum for one hour. The virus was then applied to the pretreated cells, i.e. the virus did not experience the treatment only the cells.

To confirm that the decreased CoV-2-PV entry was specific for apoE transporting lipid from the serum, we added apoE without serum and found CoV-2-PV viral entry decreased more than 50% of control (Figure 1B). The effect of cholesterol appears to be virus specific as entry of a distantly related

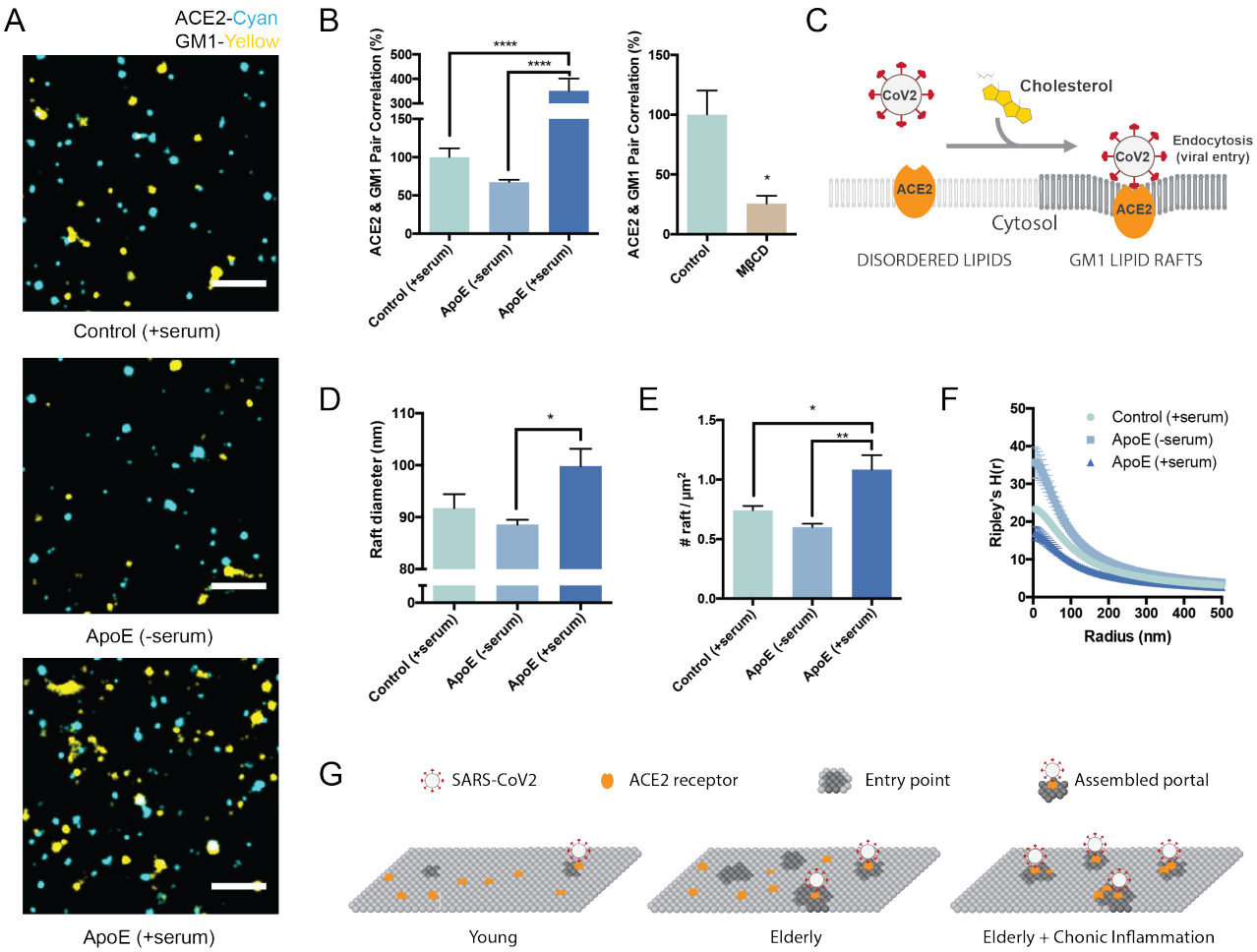


**Figure 2. Molecular basis for cholesterol dependent SARS-CoV-2 entry.** (**A**) Representative images from dSTORM super resolution imaging. GM1 lipid raft (yellow) increase dramatically in the presence of blood serum when apoE is present (bottom panel), measured by CTxB labeling. ACE2 receptor (cyan) labeled with ACE2 antibody has very little overlap with GM1 lipid rafts when blood serum is removed (middle panel). Scale bar, 1 µm. (**B**) Cholesterol dependent trafficking of ACE2 in and out of lipid rafts. ApoE-mediated cholesterol influx translocates ACE2 from disordered regions into lipid rafts while cholesterol depletion by MβCD diminishes ACE2's raft localization. (**C**) Model showing cholesterol-dependent raft localization of ACE2 enhances SARS-CoV-2 viral entry. (**D**) Raft size analysis suggests raft assembly is regulated by apoE mediated cholesterol transportation between serum and cell membrane. (**E**) ApoE transportation of cholesterol regulates raft density. Cholesterol influx from serum results in an increase in raft density. (**F**) Ripley's K-Function (H(r)) showing raft separation after cholesterol depletion while distance between rafts gets shorter as apoE transports cholesterol from serum into the membrane. (**G**) Proposed model for infectivity in SARS-CoV-2 by age and chronic disease. When cholesterol is low there are very few entry points and their diameter is small (similar to children). With age, average cholesterol levels in the tissue increase, thereby increasing the number and size of viral entry points (similar to adults). In chronically ill patients, tissue cholesterol levels are the highest and all the ACE2 receptor is positioned for viral infectivity via the more potent endocytic mechanism (adults + chronic inflammation).

control virus VSV-G had only minor effects on loading and unloading of cholesterol with apoE (Figure 1C). To further confirm the decreased viral entry is the result of cholesterol efflux, we treated cells with methyl-beta-cyclodextrin (MbCD), a chemical known to extract cholesterol from the membrane of cells. MbCD inhibited more than 90% of CoV-2-PV viral entry (Figure 1D) while having a very minimal effect on VSV-G control (Supplemental Figure S2A).

**Cholesterol dependent trafficking of the ACE2 receptor to endocytic entry point.**

The cholesterol dependence of viral entry raises the question, What molecular mechanism causes the dependence? Previous studies showed ACE2 associates with detergent resistant membranes[20], which are similar to GM1 lipid rafts, although not identical. We and many others have shown cholesterol is a major contributor to the number of and trafficking of proteins into GM1 lipid rafts in cellular membranes[27–31]. Logically, as the number of infection sites increases, there is more opportunity for viral entry.

To determine the amount of ACE2 positioned for viral entry and its dependence on cholesterol, we co-labeled ACE2 and GM1 lipid rafts in HEK293T cells with ACE2 antibody labelled with Cy3b and Alexa Fluor 647 conjugated fluorescent CTxB (a GM1 specific toxin), treated cells with apoE/serum, and imaged with super-resolution direct stochastical optical reconstruction microscopy (dSTORM)[32–35]. dSTORM is capable of visualizing nanoscale arrangements (i.e. sub-100 nm diameter lipid domain structures[36]) in intact cellular membranes.

Figure 2A shows representative dSTORM images of ACE2 and GM1 lipid rafts from apoE treated cells with and without serum exposure (i.e., cells loaded or not loaded with cholesterol, respectively). The association of ACE2 with GM1 lipid rafts was measured by pairwise correlation. Pairwise correlation measures the probability that two molecules are next to each other. For our experiments we compared the pair correlation within 0-5 nm, a very short distance.

We found pairwise correlation of ACE2 with GM1 lipid rafts increased more than 3-fold in cholesterol loaded cells. The increased correlation was not due to a change in ACE2 concentration on the cell surface (Supplemental Figure S3A-B). To confirm the effect depends on cholesterol and not another component of the serum or apoE regulation, we treated the cells with MbCD. In agreement with our viral entry assay, MbCD reduced ACE2 localization with GM1 lipid rafts by ~70%. These data suggest that cholesterol loading by apoE causes ACE2 to dock at the endocytic viral entry point (Figure 2G). We loaded cholesterol using 4 ug/mL apoE and 10% serum, the same as our viral entry assay.

We next investigated the effect cholesterol has on the number of GM1 lipid rafts in the plasma membrane (i.e., the number of viral entry points for ACE2). Using cluster analysis, we found cells loaded with cholesterol (+apoE) increased in both the number and apparent diameter of GM1 labeled rafts compared to serum only (not loaded control) (Figure 2B-C). Cholesterol depletion by MbCD also robustly decrease the apparent raft size (Figure S3C). These decreases caused lipid rafts to separate from each other measured by Ripley's H function. (See Figure 2F).

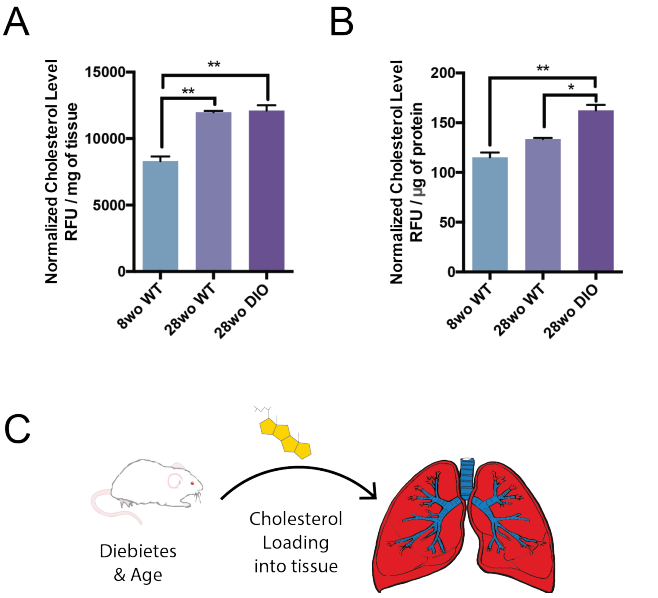


**Figure 3 Age and disease dependent cholesterol loading into mouse lung.** (**A-B**) Cholesterol measured per mg of lung tissue (A) and per µg of total proteins in the lung (B) in 8 week old (wo), 28wo mice. An aged diabetic mouse, generated by diet induced obesity (DIO), loaded ~45% more cholesterol into its lung tissue per µg of total proteins. Expressed as mean ± s.e.m., *P<0.05, **P<0.01, one-way ANOVA. (**E**) Cartoon of cholesterol (yellow shading) loaded into the lung of an aged diabetic mouse.

**Cholesterol loading into lung tissue.**

For cholesterol to have an effect *in vivo*, the cholesterol must go up in the lungs where the ACE2 expressing cells are located during an infection. To confirm age-dependent loading of cholesterol into lung tissue *in vivo*, we investigated cholesterol levels in young (8-week-old) and aged (28-week-old) C57BL/6J wild type mice. Lungs were fixed, removed, and assayed (2.5 mg of lun

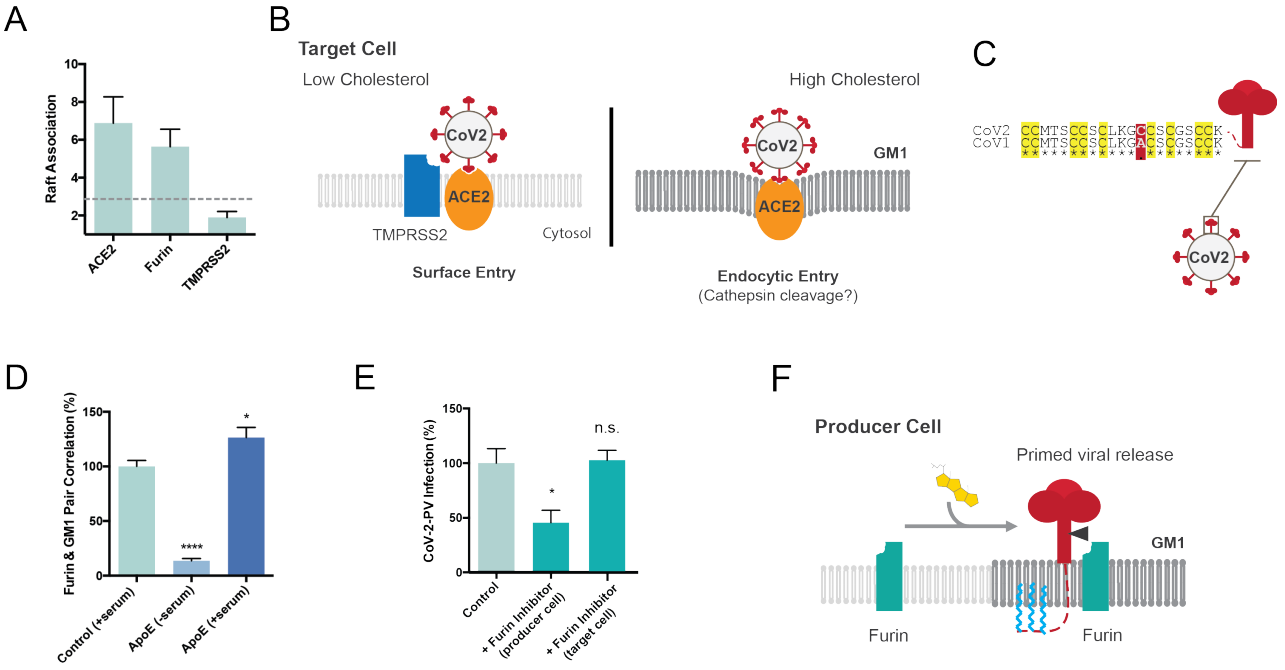


**Figure 4. Assembly of viral entrance factors in GM1 lipid rafts.** Furin and TMPRSS2 are proteases that facilitate viral entry[38,40–42]. (**A**) Super resolution imaging of ACE2, furin and TMPRSS2 with GM1 lipid rafts. Raft association is shown as a measure of pair correlation, a unitless number (see methods). A cutoff of approximately 3 times background is shown as a grey dotted line and interpreted as very little association with GM1 lipid rafts. ACE2 and furin are clearly associated with GM lipid rafts while TMPRSS2 sits in the disordered regions (<2 pair correlation with GM1 clusters). (**B**) Model showing the overall nanostructure of SARS-CoV-2 viral entry. In low cholesterol, TMPRSS2 (blue shading) and ACE2 (orange oval) are in the disordered region (light grey lipids). When the cell is loaded with cholesterol the receptor and the protease translocate to GM1 lipid rafts (GM1, dark grey lipids). The translocation has a two-fold effect. First SARS-CoV-2 is positioned with more concentrate ACE2 which can directly facilitate viral entry and putative cathepsin cleavage, second furin would be available to hydrolyze any unprimed spike protein (not shown). (**C**) Sequence alignment of the palmitoylation site in SARS-CoV-1 (GenBank: ABD72995.1) and SARS-CoV-2 (GenBank: QII57161.1). Residues conserved are marked with anasterisk. All 9 putative palmitoylation sites identified in SARS-CoV-1 are conserved in SARS-CoV-2 (yellow highlight). A single mutation introduces a 10$^{th}$ putative palmitoylation site (red shading). (**D**) Furin localization to GM1 lipid rafts is choelsterol dependent. Furin moves out of the raft under low cholesterol condition (apoE extracts cholesterol from membrane). Cholesterol loading by apoE causes an increased furin GM1 lipid pair correlation. Data are expressed as mean ± s.e.m.,*P<0.05, ****P<0.0001, one-way ANOVA. (**E**) Furin inhibitor blocks S1/S2 cleavage and virion priming during CoV-2-PV exit from producer cells, thus decreasing the efficiency for viral entry. Furin inhibitor treatment in target cells has no effect on viral entry, however when the virus is produced in the presence of a furin inhibitor, infection decreases 50%. The result suggests furin cleavage during virus production increasesr SARS-CoV-2 viral entry. Data are expressed as mean ± s.e.m., *P<0.05, n.s. P ≥0.05, two-sided Student's t-test. (**F**) Speculative role of palmitoylation in SARS-CoV-2 priming of the spike protein. In high cholesterol furin moves from the disordered lipids (light grey lipids) to ordered GM1 lipids (GM1, dark grey lipids). Cholesterol dependent membrane protein translocation is indicated by a grey arrow and the input of cholesterol (yellow shading).

tissue) for cholesterol. We found cholesterol in the lung of older adults was elevated (~45%) compared to young mice (Figure 3A). The increase was significant (P < 0.01).

Next we investigated the loading of cholesterol into lung tissue in aged (28 week) diabetic animals. We used diet induced obesity (DIO) of C57B/6J mice, a well-established mouse model for type II diabetes[37]. We noted the weight of the obese lung was increased compared to healthy lung (Supplemental Figure S2B), most likely due to increased fluid permeability due to inflammation in the diabetic mouse. To control for potential excess water in the diabetic mice, we normalized the amount of cholesterol to total protein in the tissue

homogenate. Cholesterol normalized per µg of protein was significantly elevated in DIO mice compared to both 8 week and 28 week old healthy mice (40% and 22% respectively). This level of cholesterol loading is consistent with cholesterol loading into cultured cells and suggests an age and obesity induced sensitivity to viral infection exists *in vivo*.

**Mechanism for cholesterol dependent viral entry.**

In order for the virus to enter the cell it must be primed by proteases[18]. In SARS-CoV-2 there is an efficient furin cleavage site between the S1 and S2 segments that is not found in SARS-CoV-1[38,39]. This S1/S2 site primes the virus for entry. During the preparation of pseudovirus, this site appears to be mostly cut in the producing cells[8,39]. A second site (S2') frees a fusion peptide and allows insertion of the virus into the host membrane. The S2', is thought to be cleaved by TMPRSS2 or cathepsin proteases[40–42]. In SARS-CoV-1, TMPRSS2 is associated with the cell surface entry mechanism and cathepsin is associated with the endocytic mechanism[18].

For the virus to interact with a protease it must be in proximity (i.e., the same lipid compartment). To test their potential proximity with the virus and to define the nano-scale environment, we pairwise labeled TMPRSS2 and furin in combination with GM1 lipid rafts and imaged with dSTORM. Compared to ACE2, only furin was localized to GM1 lipid rafts (Figure 4A).

Based on the positioning of ACE2 relative to TMPRSS2 and GM1 domains, we propose a model of infectivity regulated by high and low levels of cholesterol (Figure 4B). During low cholesterol ACE2 is in the disordered region and is cut by TMPRSS2, (surface entry). In high cholesterol, ACE2 translocates into the GM1 lipid raft and enters through the endocytic pathway, presumably to be cut by cathepsin similar to SARS-CoV-1.

**Role of cholesterol in furin priming.**

Next we considered palmitoylation and its role in furin priming of SARS-CoV-2 spike protein[39]. Palmitoylation is a post translation modification that attaches a 16 carbon saturated lipid to many proteins and traffics them to GM1 lipid rafts[43]. Palmitoylation of the cysteine-rich endodomain of the SARS-CoV-1 spike glycoprotein is important for spike-mediated cell fusion and viral entry[44,45]. Little is known about palmitoylation of SARS-CoV-2. We aligned SARS-CoV-1 and -2 and found that all 9 putative palmitoylation sites in SARS-CoV-1 are conserved in SARS-CoV-2 (Figure 4C). A single significant mutation (alanine to cysteine) introduces an additional putative palmitoylation site in SARS-CoV-2, which suggest SARS-CoV-2 remains under evolutionary pressure for palmitate driven viral entry.

In a virus producing cell, SARS-CoV-2 palmitoylation is positioned on the intracellular leaflet suitable for targeting the nascent spike protein to GM1 lipid rafts. To test a potential role of cholesterol in SARS-CoV-2 priming we loaded producing cells (HEK293T) with cholesterol and imaged furin trafficking in and out of lipid rafts. Cholesterol (apoE + serum) increased furin's pair correlation with GM1 lipid rafts, a location that likely favors hydrolysis of the spike protein at the S1/S2 site and facilitates priming of the virus. Unloading cholesterol from the cells (apoE - serum or MbCD) dramatically decreased the percent of furin associated with GM1 lipid rafts (Figure 4D and supplemental figure S4A).

A lack of furin priming has been shown to decrease viral entry[39] (Figure 4E). We produced CoV-2-PV in the presence of a furin specific inhibitor and tested viral entry. Consistent with other recent studies, entry was reduced ~ 50% for unprimed virus (Figure 4E). Adding the inhibitor in the target cell, after the virus is already primed, had no effect. This suggests that in low cholesterol furin is unlikely to associate with spike protein.

Figure 4F shows a speculative model for enhanced viral entry in old compared to young due to increased S1/S2 priming in virus producing cells. In young individuals the furin is trafficked outside of GM1 lipid rafts resulting in decreased access of the spike protein to furin. In high cholesterol, furin translocates into GM1 lipid rafts near furin.

**Cholesterol dependent SARS-CoV-2 receptor binding**

The reduced effectiveness of viral entry in the disordered region could be from reduced binding to

the receptor in the disordered region or reduced entry or both. To test SARS-CoV-2 binding, we applied the SARS-CoV-2 receptor binding domain (RBD) to HEK293T cells with and without MbCD. MbCD treatment reduced the binding of the RBD (Supplemental Figure 4B). However, the effect was modest and suggests viral entry rather than binding is likely more affected by cholesterol.

Lastly, we investigated whether elevated ACE2 expression has an effect on cholesterol dependent viral entry. We overexpressed ACE2 receptor and found that ACE2 pair correlation with GM1 lipid rafts substantially decreased (Supplemental Figure S4C). However, depletion of cholesterol with MbCD only modestly reduce CoV-2-PV entry (Supplemental Figure S4D). Combined these data suggest that excess ACE2 is primarily localizing to the disordered region, a result that likely increases surface entry over GM1 lipid rafts.

## DISCUSSION

Cholesterol dependence in ACE2 localization and SARS-CoV-2 entry provides a possible explanation for age sensitivity in COVID19. As mentioned, cholesterol increases in cellular tissues with age[11–13] and this accumulation directly links to disease[25] including atherosclerosis[46], and acute and chronic inflammation[14]. Remarkably, these same diseases are highly comorbid with COVID19[3,5]. Based on these finding with cholesterol, we have proposed a model for age dependent infection of SARS-CoV-2 (Figure 2G). When cholesterol is low there are very few entry points (similar to children). With age, average cholesterol levels in the tissue increase, thereby increasing the number and size of viral entry points (similar to adults). In chronically ill patients, tissue cholesterol levels are the highest and all the ACE2 receptor is positioned for viral infectivity (adults + chronic inflammation). The model is supported by age dependent loading of cholesterol into lung tissue of mice Figure 3A-B.

We conclude that SARS-CoV-2 has at least three cholesterol-dependent mechanisms that likely contribute to differential infectivity in elderly with an underlying condition and with chronic inflammation. One, number of entry sites are cholesterol dependent (Figure 2D-F). If there are few of the preferred entry points, the virus cannot enter the cell as efficiently(Figure 1B-C,). Two, the cholesterol-dependent ability of the receptor, and presumably the virus, to dock into the more advantageous lipids is logically one of the most important steps to infectivity. If the virus isn't positioned in the membrane correctly it likely cannot enter the cell through endocytosis (Figure 1B). Third, furin priming that activates SARS-CoV-2 for membrane insertion is also cholesterol dependent and likely protects against severe COVID19 symptoms (Figure 4F).

Based on the decreased efficiency of surface entry (Figure 1B-C) and the low cholesterol in lung tissue of young mice (Figure 3A), viral infection in young children is expected to be through the surface entry mechanism. Further supporting this conclusion, the increased binding of the RBD domain in higher cholesterol suggests the virus has evolved to favor the endocytic pathway (Figure 3C). Over expression of TMPRSS2 does increase infectivity[8]. If TMPRSS2 is the preferred mechanism for children, drugs that target TMPRSS2 may not be as effective in elderly and chronically ill. However, our studies cannot rule out that TMPRSS2 contributes to the endocytic pathway in pneumocytes or in higher cholesterol. Without a cholesterol source, most cell culture experiments likely represent the conditions seen in children, not the elderly and chronically ill. This may be important for development of treatments for COVID19 and studying other viruses that have cholesterol and age sensitivity.

Our model suggests high levels of cholesterol in the tissue are indicative of SARS-CoV-2 infectivity, not necessarily the levels of cholesterol in the blood. Most clinical diagnosis of cholesterol are done by analyzing blood samples, however these levels do not necessary indicate the level of cholesterol in the tissue. This difference is particularly true of chronic inflammation where blood cholesterol is low due to inhibition of cholesterol efflux proteins in the peripheral tissue[14] (see also supplementary material). Our model is consistent with a clinical study in China that showed LDL and HDL cholesterol were low in severe COVID19 patients, yet monocytes in the blood had high cholesterol[47]. The high cholesterol in monocytes is consistent with cholesterol loading into peripheral tissue during chronic inflammation.

The speculative role of palmitoylation aiding SARS-CoV-2 priming is based purely on the known affinity of palmitate for GM-1 ordered lipids[43] and

appropriately situated spike protein for cutting in a GM1 lipid raft. However, the high cholesterol could also cause furin to be endocytosed and cycled back through the Golgi where it would interact with the spike protein as it traffics to the surface of the cell. More research is needed to understand the role of palmitoylation in SARS-CoV-2 life cycle.

In our experiments, ACE2 was very sensitive to raft disruption. Previous studies used detergent resistant membranes (DRMs) to characterize localization of ACE2. Not surprisingly, conflicting reports showed ACE2 association with both disordered[48,49] and ordered lipids[20]. DRMs are a good first approximation, but for proteins that move in and out, the detergent used to prepare the DRM's likely biases proteins to the disordered regions. The use of super resolution imaging is an important advancement of this study.

Although Figure 1 shows only cholesterol controlling the trafficking of ACE2, it is likely that a specific lipid or peptide in the disordered region of the membrane influences the balance of ACE2 in or out of GM1 lipid rafts. The disordered region of the membrane is separate from GM1 lipid rafts and can have proteins or lipids that directly bind to ACE2 or palmitoylated SARS-CoV-2 and traffic ACE2 out of GM1 rafts. We have shown direct binding of phosphatidylinositol 4,5 bisphosphate ($PIP_2$) opposes localization of a palmitoylated enzyme to GM1 lipid rafts[28,50]. $PIP_2$ is polyunsaturated, cholesterol independent, and resides in the disordered region[28,51,52]. Binding of $PIP_2$ to phospholipase D counteracted its cholesterol dependent location to GM1 lipid rafts[28,53] and demonstrates that cholesterol can be in balance with other molecules in the membrane to regulate the trafficking of an enzyme in or out of a lipid raft. As cholesterol increases with age, the putative molecules that balance cholesterol also likely increase. Hence, simply removing cholesterol may have complications.

According to our model, drugs that disrupt GM1 lipid rafts, or drugs that increase cholesterol efflux, are likely the most effective for critically ill COVID19 patients. We and others have shown that polyunsaturated fatty acids oppose cholesterol signaling through GM1 lipid rafts[53]. Drugs that inhibit cholesterol synthesis could be helpful if taken over time to avoid loading tissue with cholesterol. Statins would logically be the least beneficial in late stages of chronic disease when the tissue is already loaded with cholesterol and cholesterol synthesis in the liver and transport in the blood is presumably already shut down[25].

## METHODS

### Cell culture

Human embryonic kidney 293T (HEK293T) cells and HEK293T cells overexpressing human ACE2 (hACE2) were grown in Dulbecco's Modified Eagle Medium (DMEM) containing 10% fetal bovine serum (FBS) and 1% penicillin/streptomycin.

HEK293T cells overexpressing hACE2 were generously provided by Dr. Michael Farzan (Department of Immunology and Microbiology, Scripps Research). Cells were generated by transduction with murine leukemia virus (MLV) pseudotyped with the vesicular stomatitis virus G protein and expressing myc-hACE2-c9, as previously described[54]. Briefly, HEK293T cells were co-transfected by PEI with three plasmids, pMLV-gag-pol, pCAGGS-VSV-G and pQCXIP-myc-hACE2-c9 at a ratio of 3:2:1, and medium was refreshed after overnight incubation of transfection mix. The supernatant with produced virus was harvested 72-hours post transfection and clarified by passing through 0.45µm filter. 293T-hACE2 cells were selected and maintained with medium containing puromycin (Sigma). hACE2 expression was confirmed by SARS2-PV entry assays and by immunofluorescence staining using mouse monoclonal antibody recognizing c-Myc.

### Production of SARS-CoV-2 pseudoviruses

Retroviruses pseudotyped with the SARS-CoV-2 S proteins (SARS2-PV) was produced as previously described[22,23] with modest modifications as described. HEK293T cells were transfected by X-tremeGENE™ 9 DNA Transfection Reagent (Millipore Sigma, #6365787001) at a ratio of 5:5:1 with a plasmid encoding murine leukemia virus (MLV) gag/pol proteins, a retroviral vector pQCXIX expressing firefly luciferase, and a plasmid expressing the spike protein of SARS-CoV-2 (GenBank YP_009724390) or a control plasmid (VSV-G). All the viral plasmids were provided by Dr. Michael Farzan. Cell culture supernatant containing pseudoviruses was harvested at 72 hours post transfection. For furin inhibitor

treatment, cells were incubated with 25 μM hexa-D-arginine amide (Furin Inhibitor II, Sigma-Aldrich, # SCP0148) over the process of viral production starting 6 hours after transfection.

## Viral Entry Assay

HEK293T cells were cultured in 96-well flat culture plates with transparent-bottom (Corning™ Costar™, #3585) pre-coated with poly-D-lysine. Cells were incubated with media containing 4 μg/mL apoE with or without FBS supplementation overnight before viral exposure. For MβCD treatment, cells were incubated with 100 μM MβCD for 30 min prior to virus infection. For furin inhibitor treatment, cells were incubated with 25 μM hexa-D-arginine amide for 1 hour prior to and during the whole process of virus infection.

SARS-CoV-2 pseudoviruses were applied to the cells and allowed to infect at 37 °C for 24 hours. After viral infection, efficiency of viral entry was determined through a firefly luciferase assay. Specifically, cells were washed with PBS once and 16 μL Cell Culture Lysis Reagent (Promega, #E153A) were added into each well. The plate was incubated for 15 min with rocking at room temperature. 8 μL of cell lysate from each well was added into a 384-well plate (Corning™, #3574), followed by the addition of 16 μL of Luciferase Assay Substrate (Promega, #E151A). Luciferase activity measurement was performed on a Spark 20M multimode microplate reader (Tecan). All the infection experiments were performed in a biosafety level-2 (BSL-2) laboratory.

## dSTORM Super-resolution imaging

*Fixed cell preparation*

Cells were grown to 60% confluence. Cells were incubated with 4 μg/mL purified apoE protein with or without FBS supplementation (overnight) or 100μM MβCD (30 min) in media. Cells were rinsed with PBS and then fixed with 3% paraformaldehyde and 0.1% glutaraldehyde for 20 min to fix both proteins and lipids. Fixative chemicals were reduced by incubating with 0.1% $NaBH_4$ for 7 min with shaking followed by three times 10 min washes with PBS. Cells were permeabilized with 0.2% Triton X-100 for 15 min and then blocked with a standard blocking buffer (10% bovine serum albumin (BSA) / 0.05% Triton in PBS) for 90 min at room temperature. For labelling, cells were incubated with primary antibody (anti-ACE2 antibody (Abcam, #ab189168), anti-Furin antibody (Abcam, #ab3467) or anti-TMPRSS2 antibody [EPR3861] (Abcam, #ab92323)) for 60 min in 5% BSA / 0.05% Triton / PBS at room temperature followed by 5 washes with 1% BSA / 0.05% Triton / PBS for 15 min each. Secondary antibody (donkey anti-rabbit cy3b and CTxB-647) was added in the same buffer as primary for 30 min at room temperature followed by 5 washes as stated above. Cells were then washed with PBS for 5 min. Cell labelling and washing steps were performed while shaking. Labeled cells were then post-fixed with fixing solution, as above, for 10 min without shaking followed by three 5 min washes with PBS and two 3 min washes with deionized distilled water.

*dSTORM imaging*

Images were recorded with a Zeiss ELYRA PS.1 microscope using TIRF mode equipped with a pil-immersion 63x objective. Andor iXon 897 EMCCD camera was used along with the Zen 10D software for image acquisition and processing. The TIRF mode in the dSTORM imaging provided low background high-resolution images of the membrane. A total of 10,000 frames with an exposure time of 18 ms were collected for each acquisition. Excitation of the Alexa Fluor 647 dye was achieved using 642 nm lasers and Cy3B was achieved using 561 nm lasers. Cells and brain tissues were imaged in a photo-switching buffer comprising of 1% β-mercaptoethanol (Sigma, #63689), and oxygen scavengers (glucose oxidase (Sigma, #G2133) and catalase (Sigma, #C40)) in 50mM Tris (Affymetrix, #22638100) + 10mM NaCl (Sigma, #S7653) + 10% glucose (Sigma, #G8270) at pH 8.0. Sample drift during acquisition was corrected by an autocorrelative algorithm.

Images were constructed using the default modules in the Zen software. Each detected event was fitted to a 2D Gaussian distribution to determine the center of each point spread function plus the localization precision. The Zen software also has many rendering options including removing localization errors and outliers based on brightness and size of fluorescent signals. Pair correlation and cluster analysis was performed using the Statistical Analysis package in the Vutara SRX software. Pair Correlation analysis is a

statistical method used to determine the strength of correlation between two objects by counting the number of points of probe 2 within a certain donut-radius of each point of probe 1. This allows for localization to be determined without overlapping pixels as done in traditional diffraction-limited microscopy. Raft size estimation and raft density were calculated through cluster analysis by measuring the length and density of the clusters comprising of more than 10 particles with a maximum particle distance of 0.1 µm. Ripley's H(r) analysis was performed to study the distribution of lipid raft clusters.

### Lung cholesterol assay

To measure the relative changes in cholesterol level in lung tissue, we developed an Amplex Red-based cholesterol assay. Lungs were removed from C57BL/6J wild type and diet induced obesity (DIO) mice.__Housing, animal care and experimental procedures were consistent with the Guide for the Care and Use of Laboratory Animals and approved by the Institutional Animal Care and Use Committee of the Scripps Research Institute. The left lobe of each lung was homogenized with RIPA lysis buffer. After centrifugation, supernatant were collected for cholesterol and protein measurement. 50 µL of supernatant were mixed with 50 µL of assay solution containing 100 µM Amplex red, 2 U/mL horseradish peroxidase, 4 U/mL cholesterol oxidase and 4 U/mL cholesteryl esterase in PBS in 96-well plates with transparent-bottom (Corning™ Costar™, #3585). Relative cholesterol concentration was determined for each sample by measuring fluorescence activity with a fluorescence microplate reader (Tecan Infinite 200 PRO, reading from bottom) with excitation wavelength of 530 nm and an emission wavelength of 585 nm. Subsequently, cholesterol level was normalized by tissue weights and protein concentration. Cholesterol signals were then graphed (Mean ± s.e.m.) and statistically analyzed (one-way ANOVA) with GraphPad Prism software (v6.0f).

### Receptor Binding Domain (RBD) Binding Assay

HEK293T cells were seeded into 96-well flat culture plates with transparent-bottom (Corning™ Costar™, #3585) one day before experiment. SARS-CoV-2 RBD with a human Fc fusion was a generous gift from Dr. Michael Farzan (Department of Immunology and Microbiology, Scripps Research). HEK293T cells were incubated with 10 µg/mL RBD peptide in cell culture medium overnight at 37°C in 5% $CO_2$. Cells were washed with PBS once before fixation with 3% paraformaldehyde. After blocking with a standard blocking buffer (10% bovine serum albumin (BSA) / 0.05% Triton in PBS) for 90 min at room temperature, RBD binding to the cells were labelled with Alexa 647 goat anti-human IgG (Jackson ImmunoResearch, # 109-606-098) for 6 hours at 4°C. After labelling, cells were washed with PBS twice. Relative RBD binding was determined in quintuplicate for each condition by measuring fluorescent activity with a fluorescence microplate reader (Tecan Infinite 200 PRO) with excitation wavelength of 630 nm and an emission wavelength of 680 nm.

### Statistical Analyses

All statistical calculations were performed in GraphPad Prism v6.0. For the Student's t test, significance was calculated using a two-tailed unpaired parametric test with significance defined as $p < 0.05$, **P<0.01, ***P<0.001, ****P<0.0001. For the multiple comparison test, significance was calculated using an ordinary one-way ANOVA with Dunnett's multiple comparisons test.

### Acknowledgements

We thank Michael Farzan for the SARS-CoV-2 spike plasmid, hACE2 overexpression HEK293T cell line, and RBD peptide; Andrew S. Hansen for helpful discussion and reading of the manuscript. This work was supported by the National Institutes of Health via a Director's New Innovator Award to S.B.H. (DP2NS087943), R01 to S.B.H. (R01NS112534). We are grateful to the Iris and Junming Le Foundation for funds to purchase a super-resolution microscope, making this study possible.

**References**


1. Wu, Z. & McGoogan, J. M. Characteristics of and Important Lessons from the Coronavirus Disease 2019 (COVID-19) Outbreak in China: Summary of a Report of 72314 Cases from the Chinese Center for Disease Control and Prevention. *JAMA - J. Am. Med. Assoc.* **323**, 13–16 (2020).
2. Wu, J. T. *et al.* Estimating clinical severity of COVID-19 from the transmission dynamics in Wuhan, China. *Nat. Med.* **26**, (2020).
3. Yang, J. *et al.* Prevalence of comorbidities in the novel Wuhan coronavirus (COVID-19) infection: a systematic review and meta-analysis. *Int. J. Infect. Dis.* **94**, 91–95 (2020).
4. Chen, T. *et al.* Clinical characteristics of 113 deceased patients with coronavirus disease 2019: retrospective study. *BMJ* **368**, m1091 (2020).
5. Gentile, S., Strollo, F. & Ceriello, A. COVID-19 Infection in italian people with diabetes: lessons learned for our future (an experience to be used). *Diabetes Res. Clin. Pract.* **162**, 108137 (2020).
6. Stockman, L. J. *et al.* Severe acute respiratory syndrome in children. *Pediatr. Infect. Dis. J.* **26**, 68–74 (2007).
7. Li, W. *et al.* Angiotensin-converting enzyme 2 is a functional receptor for the SARS coronavirus. *Nature* **426**, 450–4 (2003).
8. Hoffmann, M. *et al.* SARS-CoV-2 Cell Entry Depends on ACE2 and TMPRSS2 and Is Blocked by a Clinically Proven Protease Inhibitor. *Cell* **181**, 271-280.e8 (2020).
9. Jia, H. P. *et al.* ACE2 Receptor Expression and Severe Acute Respiratory Syndrome Coronavirus Infection Depend on Differentiation of Human Airway Epithelia. *J. Virol.* **79**, 14614–14621 (2005).
10. Bezara, M. ortiz *et al.* Heterogeneous expression of the SARS-Coronavirus-2 receptor ACE2 in the human respiratory tract. 1–13 (2020). doi:doi.org/10.1101/2020.04.22.056127
11. Angel, A. & Farkas, J. Regulation of cholesterol storage in adipose tissue. *J. Lipid Res.* **15**, 491–499 (1974).
12. Adams, C. W., Bayliss, O. B., Baker, R. W., Abdulla, Y. H. & Hunter-Craig, C. J. Lipid deposits in ageing human arteries, tendons and fascia. *Atherosclerosis* **19**, 429–40 (1974).
13. Sene, A. *et al.* Impaired cholesterol efflux in senescent macrophages promotes age-related macular degeneration. *Cell Metab.* **17**, 549–561 (2013).
14. Tall, A. R. & Yvan-Charvet, L. Cholesterol, inflammation and innate immunity. *Nat. Rev. Immunol.* **15**, 104–116 (2015).
15. Gowdy, K. M. & Fessler, M. B. Emerging roles for cholesterol and lipoproteins in lung disease. *Pulm. Pharmacol. Ther.* **26**, 430–7 (2013).
16. Fessler, M. B. A new frontier in immunometabolism cholesterol in lung health and disease. *Ann. Am. Thorac. Soc.* **14**, S399–S405 (2017).
17. Andersson, J. M., Grey, C., Larsson, M., Ferreira, T. M. & Sparr, E. Effect of cholesterol on the molecular structure and transitions in a clinical-grade lung surfactant extract. *Proc. Natl. Acad. Sci. U. S. A.* **114**, E3592–E3601 (2017).
18. Simmons, G., Zmora, P., Gierer, S., Heurich, A. & Pöhlmann, S. Proteolytic activation of the SARS-coronavirus spike protein: Cutting enzymes at the cutting edge of antiviral research. *Antiviral Research* **100**, 605–614 (2013).
19. Lingwood, D. & Simons, K. Lipid rafts as a membrane-organizing principle. *Science* **327**, 46–50 (2010).
20. Lu, Y., Liu, D. X. & Tam, J. P. Lipid rafts are involved in SARS-CoV entry into Vero E6 cells. *Biochem. Biophys. Res. Commun.* **369**, 344–349 (2008).
21. Glende, J. *et al.* Importance of cholesterol-rich membrane microdomains in the interaction of the S protein of SARS-coronavirus with the cellular receptor angiotensin-converting enzyme 2. *Virology* **381**, 215–221 (2008).
22. Quinlan, B. D. *et al.* The SARS-CoV-2 receptor-binding domain elicits a potent neutralizing resonse without antibody-dependent enhancement. *bioRxiv* 1–9 (2020). doi:10.1101/2020.04.10.036418
23. Moore, M. J. *et al.* Retroviruses Pseudotyped with the Severe Acute Respiratory Syndrome Coronavirus Spike Protein Efficiently Infect Cells Expressing Angiotensin-Converting Enzyme 2. *J. Virol.* **78**, 10628–10635 (2004).
24. Wong, S. K., Li, W., Moore, M. J., Choe, H. & Farzan, M. A 193-Amino Acid Fragment of the SARS Coronavirus S Protein Efficiently Binds Angiotensin-converting Enzyme 2. *J. Biol. Chem.* **279**, 3197–3201 (2004).
25. Luo, J., Yang, H. & Song, B. L. Mechanisms and regulation of cholesterol homeostasis. *Nat. Rev. Mol. Cell Biol.* **21**, 225–245 (2020).
26. Kuo, C.-L. *et al.* APOE e4 genotype predicts severe COVID-19 in the UK Biobank community cohort. *Journals Gerontol. Ser. A* 1–29 (2020). doi:10.1093/gerona/glaa131
27. Sezgin, E., Levental, I., Mayor, S. & Eggeling, C. The mystery of membrane organization: composition, regulation and roles of lipid rafts. *Nat. Rev. Mol. Cell Biol.* **18**, 361–374 (2017).
28. Petersen, E. N., Chung, H.-W., Nayebosadri, A. & Hansen, S. B. Kinetic disruption of lipid rafts is a

mechanosensor for phospholipase D. *Nat. Commun.* **7**, 13873 (2016).
29. Pavel, M. A. M. A., Chung, H. H.-W., Petersen, E. N. N. & Hansen, S. B. S. B. Polymodal Mechanism for TWIK-Related K+ Channel Inhibition by Local Anesthetic. *Anesth. Analg.* **129**, 973–982 (2019).
30. Pavel, M. A., Petersen, E. N., Lerner, R. A. & Hansen, S. B. Studies on the mechanism of general anesthesia. *PNAS* **in press**, (2020).
31. Petersen, E. N., Pavel, M. A., Wang, H. & Hansen, S. B. Disruption of palmitate-mediated localization; a shared pathway of force and anesthetic activation of TREK-1 channels. *Biochim. Biophys. Acta - Biomembr.* **1862**, 183091 (2020).
32. Jones, S. a, Shim, S.-H., He, J. & Zhuang, X. Fast, three-dimensional super-resolution imaging of live cells. *Nat. Methods* **8**, 499–508 (2011).
33. Huang, B., Wang, W., Bates, M. & Zhuang, X. Three-dimensional super-resolution imaging by stochastic optical reconstruction microscopy. *Science* **319**, 810–3 (2008).
34. Betzig, E. *et al.* Imaging intracellular fluorescent proteins at nanometer resolution. *Science* **313**, 1642–1645 (2006).
35. Hess, S. T., Girirajan, T. P. K. K. & Mason, M. D. Ultra-high resolution imaging by fluorescence photoactivation localization microscopy. *Biophys. J.* **91**, 4258–4272 (2006).
36. Honigmann, A. *et al.* Scanning STED-FcS reveals spatiotemporal heterogeneity of lipid interaction in the plasma membrane of living cells. *Nat. Commun.* **5**, (2014).
37. Wang, C.-Y. & Liao, J. K. A mouse model of diet-induced obesity and insulin resistance. *Methods Mol. Biol.* **821**, 421–33 (2012).
38. Coutard, B. *et al.* The spike glycoprotein of the new coronavirus 2019-nCoV contains a furin-like cleavage site absent in CoV of the same clade. *Antiviral Research* **176**, (2020).
39. Hoffmann, M., Kleine-Weber, H. & Pöhlmann, S. A Multibasic Cleavage Site in the Spike Protein of SARS-CoV-2 Is Essential for Infection of Human Lung Cells. *Mol. Cell* **78**, 779-784.e5 (2020).
40. Glowacka, I. *et al.* Evidence that TMPRSS2 Activates the Severe Acute Respiratory Syndrome Coronavirus Spike Protein for Membrane Fusion and Reduces Viral Control by the Humoral Immune Response. *J. Virol.* **85**, 4122–4134 (2011).
41. Huang, I. C. *et al.* SARS coronavirus, but not human coronavirus NL63, utilizes cathepsin L to infect ACE2-expressing cells. *J. Biol. Chem.* **281**, 3198–3203 (2006).
42. Millet, J. K. & Whittaker, G. R. Host cell proteases: Critical determinants of coronavirus tropism and pathogenesis. *Virus Research* **202**, 120–134 (2015).
43. Levental, I., Lingwood, D., Grzybek, M., Coskun, U. & Simons, K. Palmitoylation regulates raft affinity for the majority of integral raft proteins. *Proc. Natl. Acad. Sci.* **107**, 22050–22054 (2010).
44. Petit, C. M. *et al.* Palmitoylation of the cysteine-rich endodomain of the SARS-coronavirus spike glycoprotein is important for spike-mediated cell fusion. *Virology* **360**, 264–274 (2007).
45. McBride, C. E. & Machamer, C. E. Palmitoylation of SARS-CoV S protein is necessary for partitioning into detergent-resistant membranes and cell-cell fusion but not interaction with M protein. *Virology* **405**, 139–148 (2010).
46. Linton, M. F. *et al. The Role of Lipids and Lipoproteins in Atherosclerosis*. *Endotext* (2000).
47. Hu, X., Chen, D., Wu, L., He, G. & Ye, W. Low Serum Cholesterol Level Among Patients with COVID-19 Infection in Wenzhou, China. *SSRN Electron. J.* (2020). doi:10.2139/ssrn.3544826
48. Warner, F. J. *et al.* Angiotensin-converting enzyme 2 (ACE2), but not ACE, is preferentially localized to the apical surface of polarized kidney cells. *J. Biol. Chem.* **280**, 39353–39362 (2005).
49. Li, G. M., Li, Y. G., Yamate, M., Li, S. M. & Ikuta, K. Lipid rafts play an important role in the early stage of severe acute respiratory syndrome-coronavirus life cycle. *Microbes Infect.* **9**, 96–102 (2007).
50. Robinson, C. V., Rohacs, T. & Hansen, S. B. Tools for Understanding Nanoscale Lipid Regulation of Ion Channels. *Trends Biochem. Sci.* **44**, 795–806 (2019).
51. van den Bogaart, G. *et al.* Membrane protein sequestering by ionic protein-lipid interactions. *Nature* **479**, 552–5 (2011).
52. Wang, J. & Richards, D. a. Segregation of PIP2 and PIP3 into distinct nanoscale regions within the plasma membrane. *Biol. Open* **1**, 857–62 (2012).
53. Nayebosadri, A., Petersen, E. N., Cabanos, C. & Hansen, S. B. A Membrane Thickness Sensor in TREK-1 Channels Transduces Mechanical Force. *SSRN Electron. J.* (2018). doi:10.2139/ssrn.3155650
54. Wicht, O. *et al.* Identification and Characterization of a Proteolytically Primed Form of the Murine Coronavirus Spike Proteins after Fusion with the Target Cell. *J. Virol.* (2014). doi:10.1128/jvi.03451-13

## Supplemental Figures

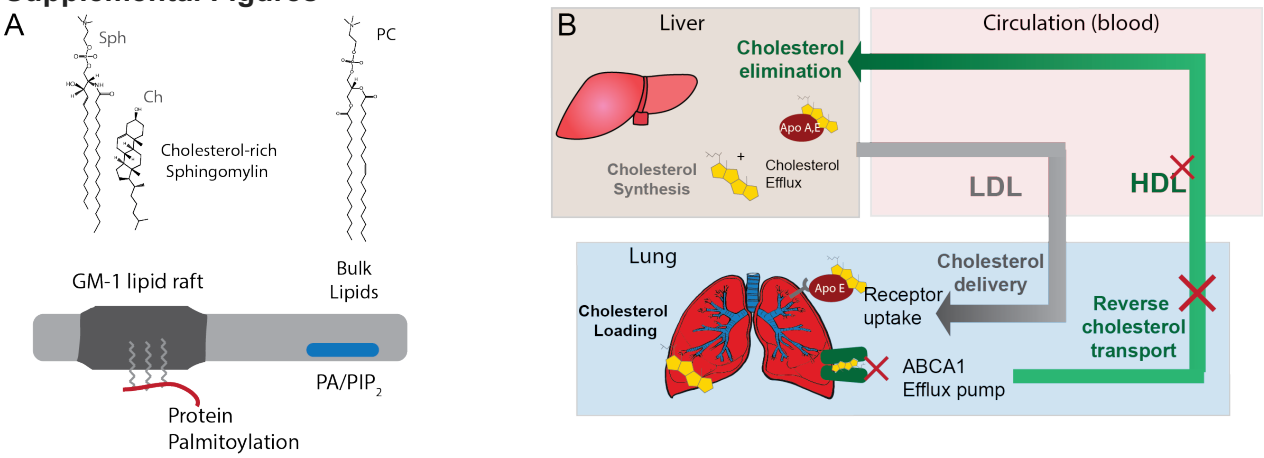


**Figure S1.** Cholesterol transport and function in GM1 lipid rafts (**A**) The side view of a plasma membrane is shown (top extracellular). The membrane partitions into regions of ordered (saturated) and disordered (unsaturated) lipids. The ordered region contains cholesterol and sphingolipids (Sph). Packing of cholesterol with saturated lipids is thought to provide order and makes ordered lipids thicker than disordered lipids. The disordered region contains unsaturated lipids including phosphatidylcholine (PC), phosphatidic acid (PA), and phosphatidylinositol 4,5-bisphosphate ($PIP_2$). $PIP_2$ and PA are signaling lipids and $PIP_2$ forms its own lipid domains separate from GM1 lipid rafts. Palmitoylation of proteins typically occurs on the cytosolic portion of the membrane and inserts into the inner leaflet (red line with lipids attached). For a virus that exits the cell the palmitoylation may insert into the extracellular leaflet. (**B**) Cholesterol loading into lung pneumocyte's and macrophages. In healthy individuals most cholesterol is produced in the liver. Cholesterol effluxes through ATP binding cassette (ABC) transporters (not shown) and is loaded into apolipoproteins (e.g., A and E; apoA and apoE). The cholesterol is then transported through the blood serum in the form of high- and low- density lipoproteins to the lung. In the lung receptors take up the cholesterol. In healthy individuals, excess cholesterol is effluxed from ABCA1 transporter in the lung loaded into apoA1 or apoE and transported back to the liver for elimination. During chronic inflammation reverse cholesterol transport is inhibited and cholesterol is loaded into macrophage rich tissues in the periphery.

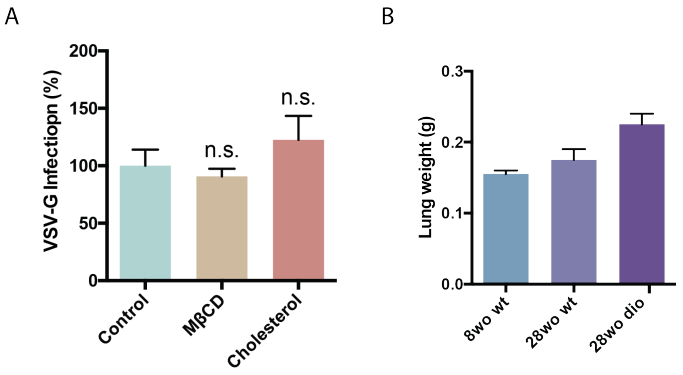


**Figure S2.** VSV-G viral entry and lung weight. (**A**) Cells were treated with MβCD and a luciferase expressing retrovirus pseudotyped with the VSV-G spike protein. VSV-G is a similar but distant virus compared to SARS-CoV-2 and serves as a control for age-dependent cholesterol selectivity. Infectivity was monitored by a luciferase activity in cells treated with methyl-beta-cyclodextrin (MβCD) or MβCD with cholesterol. Data are expressed as mean ± s.e.m., n.s.>0.05 , one-way ANOVA. (**B**) Lung weight per mg of lung tissue. Lungs were extracted from 8-week-old (wo) and 28wo mice, fixed and assayed for cholesterol with a fluorescent assay, Student's T test (*P<0.05 n=2).

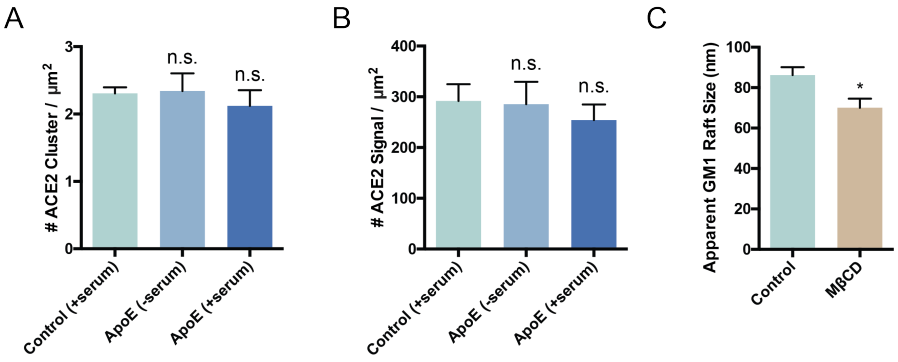


**Figure S3.** ACE2 surface expression and GM1 lipid raft density. Quantitation of ACE2 cluster (**A**) and signal (**B**) shows that the expression of ACE2 remains roughly constant when cells are loaded or unloaded with cholesterol by the cholesterol transport protein apoE. Although, while not statistically significant ACE2 expression appears to slightly decrease in high cholesterol (ApoE + serum) which agrees with the clinical findings of decreased ACE2 surface expression in older people. Data are expressed as mean ± s.e.m.,*P<0.05, one-way ANOVA. (**C**) Cholesterol depletion by methyl-beta-cyclodextrin (MβCD) robustly decreases the apparent size of GM1 lipid rafts. Data are expressed as mean ± s.e.m., *P<0.05, two-sided Student's t-test.

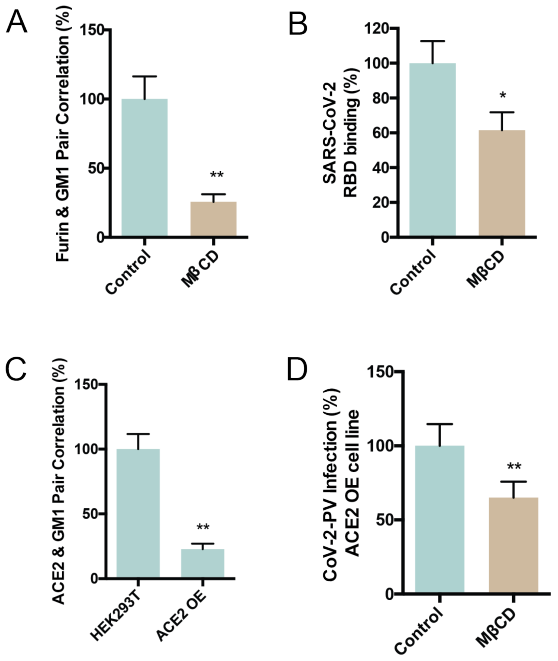


**Figure S4** Effects of MβCD on Furin, RBD, and ACE2 Over expression (**A**) Cholesterol depletion by MβCD traffics furin out of the GM1 lipid rafts into disordered regions. Data are expressed as mean ± s.e.m., **P<0.01, two-sided Student's t-test. (**B**) The receptor binding domains (RBD) of SARS-CoV-2 was added to cells treated with or without methyl-beta-cyclodextrin (MβCD). Binding was measured by fluorescence from an Alexa 647 labeled antibody to an FC tag on the RBD protein. (**C**) Overexpression of ACE2 decreases ACE2 pair correlation with GM1 lipid rafts suggesting additional ACE2 is added primarily to the disordered region, not GM1 lipid rafts. Data are expressed as mean ± s.e.m., *P<0.05, **P<0.01, two-sided Student's t-test. (**D**) Depletion of cellular cholesterol with methyl-beta-cyclodextrin (MβCD) in ACE2 overexpression (OE) HEK293T cells blocked viral entry measured by pseudotyped luciferase assay. Data are expressed as mean ± s.e.m., **P<0.01, two-sided Student's t-test.